Photoanodes

DOI: 10.1002/anie.201207578

A Three-Dimensional Branched Cobalt-Doped α-Fe_2O_3 Nanorod/$MgFe_2O_4$ Heterojunction Array as a Flexible Photoanode for Efficient Photoelectrochemical Water Oxidation**

*Yang Hou, Fan Zuo, Alex Dagg, and Pingyun Feng**

With a rising global energy demand and subsequent need for new energy sources, photoelectrochemical (PEC) water splitting using semiconductors and solar energy has received considerable attention.[1] α-Fe_2O_3 is a promising semiconductor because of its stability, favorable band gap, abundance, and low cost.[2] However, its low photoconversion efficiency restricts its practical application. Various strategies such as tailoring the morphology,[3] impurity doping,[4] and heterojunction construction[5] have been developed to enhance the photoconversion efficiency.

Recent work with morphology tailoring has focused on 3D branched (3DB) nanorod/nanowire arrays. Such an architecture offers a long optical path for effective light harvesting, short diffusion distance for excellent charge transport, and large surface area for fast interfacial charge collection. However, most of the reported 3DB nanomaterials (for example, TiO_2 nanorods,[6] TiO_2 nanorods/Si,[7] ZnO nanowires/Si[8]) possess a large band gap that prevent efficient absorption of visible light, thus decreasing overall efficiency. Therefore, it is highly desirable to develop 3DB nanomaterials that respond to visible light; 3DB α-Fe_2O_3 is a promising candidate because of the aforementioned advantages.

To enhance PEC performance, impurity doping is a widely adopted strategy. Co^{2+} is a suitable dopant for α-Fe_2O_3 because it could be incorporated into the crystal lattice of Fe_2O_3, thus easily forming a doping energy level and leading to the narrowed band gap and reduced charge carrier recombination.[9]

Moreover, coupling of Fe_2O_3 with other semiconductors to form a heterojunction is also effective strategy that enhances the separation of electron–hole pairs and improves the photoconversion efficiency.[10] Among various semiconductors, spinel $MgFe_2O_4$ is probably one of the most ideal candidates owing to its moderate band gap (2.0 eV) and suitable band-edge positions, which match well with hematite when forming a heterojunction. Also, it has a good photochemical stability, which leads to resistance to photocorrosion.[11] To our knowledge, there has been no study on the construction of a 3DB Fe_2O_3-based heterojunction with visible-light-response.

Herein, we present the synthesis and characterization of a 3DB Co-doped Fe_2O_3 nanorod array (Co-Fe_2O_3-NA)/$MgFe_2O_4$ heterojunction for efficient PEC water oxidation. The 3DB heterojunction was prepared by hydrothermal deposition of Co-Fe_2O_3-NA on Ti mesh, with subsequent coating of $MgFe_2O_4$ by a simple wet impregnation, followed by annealing (see the Supporting Information for details).

The synthesized 3DB Co-Fe_2O_3-NA/$MgFe_2O_4$ heterojunction was investigated by X-ray diffraction (Supporting Information, Figure S1), which revealed the coexistence of rhombohedral Co-Fe_2O_3-NA (JCPDS 33-0664) and spinel $MgFe_2O_4$ (JCPDS 71-1232). The average crystallite size of $MgFe_2O_4$ calculated from the width of the (220) crystal face using Scherrer's equation,[12] is about 15 nm, which is consistent with the TEM analysis. A slight shift of the (012) peak of Co-Fe_2O_3-NA to a lower angle is observed owing to the partial substitution of Fe sites by Co ions. The difference in ionic radii of Fe^{3+} (0.64 Å) and Co^{2+} (0.74 Å) causes changes in lattice parameters, indicating larger Co ions have successfully entered into the lattice of Fe_2O_3. The Raman spectrum recorded from the heterojunction (Supporting Information, Figure S2) exhibits six intense bands located at 221, 282, 338, 417, 492, and 606 cm^{-1}. Two bands at 338 and 492 cm^{-1} match spinel $MgFe_2O_4$,[13] while the other bands agree well with the A_{1g}, E_g, E_g and E_g vibrational modes of rhombohedral Co-Fe_2O_3-NA, which further confirm that the 3DB Co-Fe_2O_3-NA/$MgFe_2O_4$ heterojunction is composed of Co-Fe_2O_3-NA and $MgFe_2O_4$. Furthermore, XPS results also demonstrate the existence of Mg^{2+} (Mg 1s peak at 1303.0 eV), Fe^{3+} (Fe 2p peaks at 710.5 and 724.2 eV), Co^{2+} (Co 3p peak at 62.3 eV), and C (C 1s peak at 284.6 eV) in the 3DB Co-Fe_2O_3-NA/$MgFe_2O_4$ heterojunction (Supporting Information, Figure S3). The C signal is attributed to carbon fabric and adventitious carbon.

The Ti meshes used before and after growing the heterojunction are shown in Figure 1 a,b. The Ti mesh changes from a silver to red color during the reaction because a layer of Co-Fe_2O_3-NA/$MgFe_2O_4$ heterojunction formed on the mesh surface (Supporting Information, Figure S4). After reaction, the mesh shows good flexibility owing to the mechanical properties of the Ti mesh substrate (Figure 1 c). Figure 1 d–h shows surface and cross-sectional FESEM images of untreated Ti mesh and Co-Fe_2O_3-NA grown on the Ti mesh. It is clearly seen that after hydrothermal treatment, a highly dense and uniform Co-Fe_2O_3-NA was grown perpendicular to the surface of Ti mesh. The nanorods

[*] Dr. Y. Hou, Dr. F. Zuo, A. Dagg, Prof. Dr. P. Y. Feng
Department of Chemistry, University of California
Riverside, CA 92521 (USA)
E-mail: pingyun.feng@ucr.edu

[**] We are grateful for support of this work by the NSF (CHE-1213795 and DMR-0958796).

Supporting information for this article is available on the WWW under http://dx.doi.org/10.1002/anie.201207578.

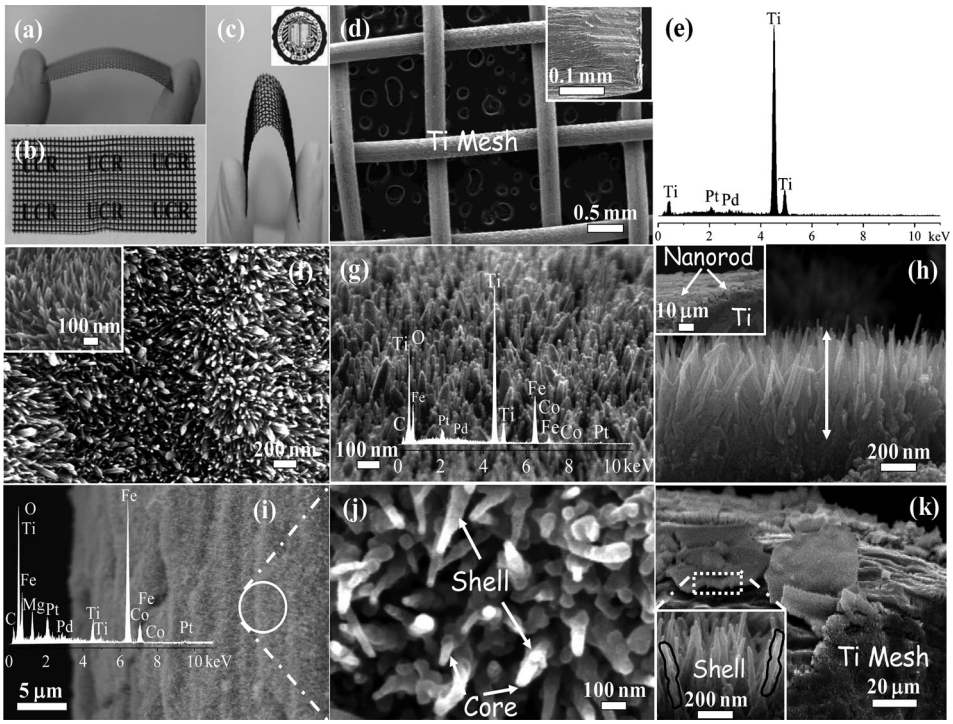

Figure 1. Photographs of the Ti mesh before (a) and after growing with Co-Fe_2O_3-NA/$MgFe_2O_4$ heterojunction (b–c). FESEM images of the Ti mesh (d), Co-Fe_2O_3-NA (f–h) and Co-Fe_2O_3-NA/$MgFe_2O_4$ heterojunction (i–k). The corresponding EDX spectra are shown in (e), (g), and (i). An enlarged version of the figure is also shown in the Supporting Information, Figure S4.

grew radially outward around the entire surface of the Ti wire to form a branched 3D structure (inset of Figure 1h). They are uniformly and tightly packed, and have a uniform diameter and length of 50 nm and 400 nm, respectively. Such an architecture could have larger surface area, better charge transport, and more efficient light absorption properties than traditional 1D films.[6,7] The outer layer of $MgFe_2O_4$ deposited uniformly as a shell on the Co-Fe_2O_3-NA core without any separately grown nanoparticles (Figure 1i,j). All of the Co-Fe_2O_3-NA remained straight and no agglomeration was observed after $MgFe_2O_4$ growth. Closer observation reveals that the 3DB Co-Fe_2O_3-NA/$MgFe_2O_4$ heterojunction exhibits a larger diameter and rougher surface than that of bare Co-Fe_2O_3-NA (Figure 1j,k). Moreover, an EDX spectrum (inset of Figure 1i) reveals that the heterojunction is composed of the elements of Fe, Mg, Co, Ti, and O.

Further information about the microstructure of the 3DB Co-Fe_2O_3-NA/$MgFe_2O_4$ heterojunction was obtained from TEM and HRTEM images. Enlarged TEM images (Figure 2d,e) show that the $MgFe_2O_4$ shells have a thickness of about 20 nm and they are uniform along the entire length of the straight Co-Fe_2O_3-NA. This suggests that an intimate and coherent interface was formed with the nanorod core. This is important for improving charge separation and thus PEC activity. A HRTEM image (Figure 2f) taken from the circled area of Figure 2e reveals clear lattice fringe spacings of 0.252 and 0.298 nm, which agrees well with the (110) plane of Co-Fe_2O_3-NA (JCPDS 1-1053) and (220) plane of $MgFe_2O_4$ (JCPDS 73-1720), respectively.

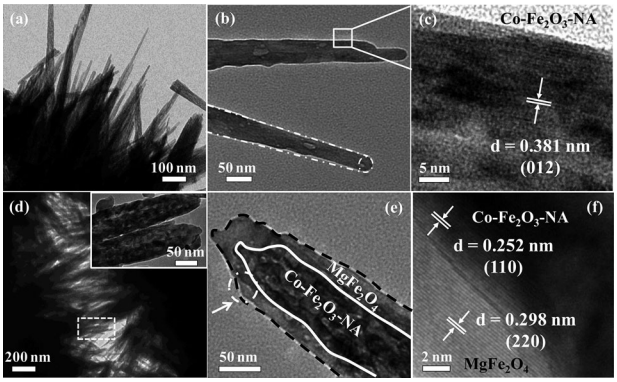

Figure 2. TEM and HRTEM images of the Co-Fe_2O_3-NA (a–c) and Co-Fe_2O_3-NA/$MgFe_2O_4$ heterojunction (d–f).

UV/Vis diffuse reflectance spectra of the samples are shown in the Supporting Information, Figure S5. The absorption edge of 3DB Co-Fe_2O_3-NA is slightly red-shifted compared with bare 3DB Fe_2O_3-NA. This could be contributed to the cobalt doping in Fe_2O_3.[14] Significant enhancement in light absorption intensity and an obvious red-shift of the absorption edge are observed for the 3DB Co-Fe_2O_3-NA/$MgFe_2O_4$ heterojunction, indicating that the loading of $MgFe_2O_4$ further improves the light absorption ability of the composite owing to its lower band gap ($MgFe_2O_4$, 2.0 eV).

Figure 3a compares plots of photocurrent density versus potential for Fe_2O_3-NA, Co-Fe_2O_3-NA, and the Co-Fe_2O_3-NA/$MgFe_2O_4$ heterojunction under chopped simulated sunlight irradiation (100 mW cm^{-2}, AM 1.5G). The measured potentials versus Ag/AgCl were adjusted to the reversible hydrogen electrode (RHE) scale according to the Nernst equation, $E_{RHE} = E_{(Ag/AgCl)} + 0.6$ V.[15] The dark current densities in all cases can be negated. Upon irradiation, the Fe_2O_3-NA yielded a photocurrent density of 1.24 mA cm^{-2} at 0.8 V (1.4 V vs. RHE). To our knowledge, this is the highest photocurrent density reported for pure Fe_2O_3 film.[16] More impressively, the Co-Fe_2O_3-NA/$MgFe_2O_4$ heterojunction showed a large enhancement in photoresponse with a photocurrent density of 3.34 mA cm^{-2} at the same applied voltage, which is about 2.69 and 1.95 times larger than those of Fe_2O_3-NA and Co-Fe_2O_3-NA (1.71 mA cm^{-2}), respectively. The

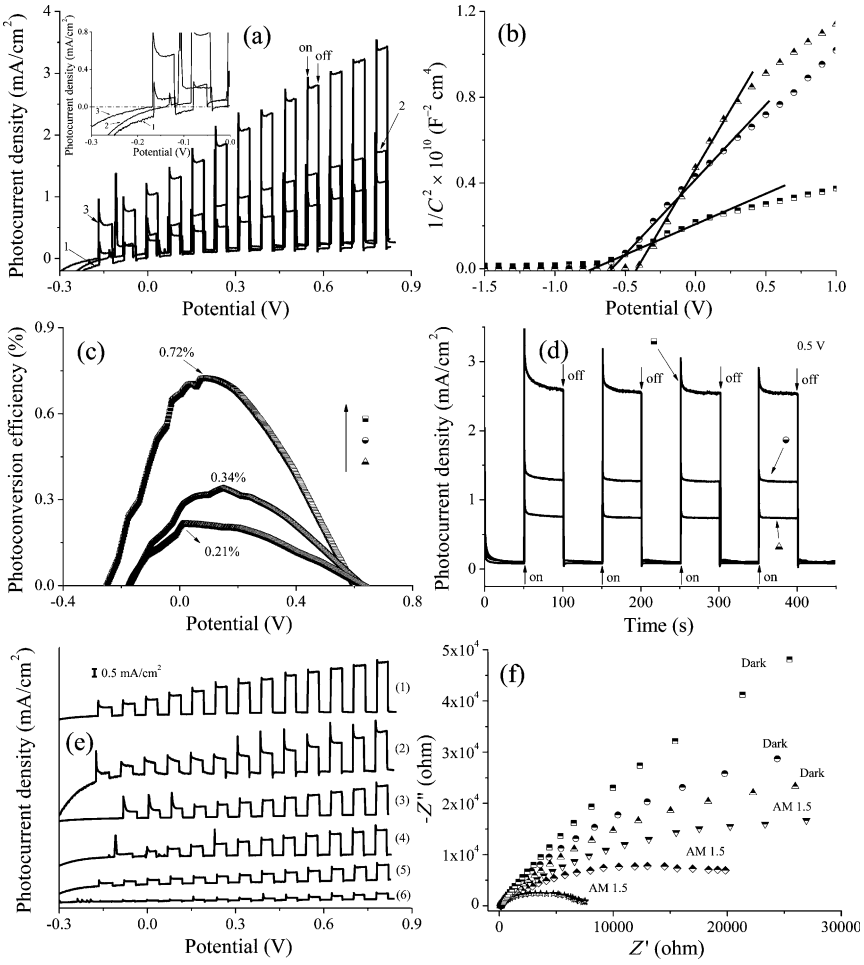

Figure 3. a) Variation of photocurrent density versus applied voltage, b) Mott–Schottky plots, c) photoconversion efficiency as a function of applied potential, and d) transient photocurrent density versus time plotted for Fe_2O_3-NA (1, △), Co-Fe_2O_3-NA (2, ○), and Co-Fe_2O_3-NA/$MgFe_2O_4$ heterojunction (3, □) in 0.01 M Na_2SO_4 electrolyte under simulated sunlight irradiation. e) Current–potential plots for Co-Fe_2O_3-NA/$MgFe_2O_4$ heterojunction (1), Fe_2O_3-NA/$MgFe_2O_4$ (2), 1D Co-Fe_2O_3-NA/$MgFe_2O_4$ heterojunction (3), Co-Fe_2O_3-NA (4), Fe_2O_3-NA (5), and $MgFe_2O_4$ (6) irradiated with chopped simulated sunlight. f) EIS Nynquist plots of the Fe_2O_3-NA (□, ▽), Co-Fe_2O_3-NA (○, ◇) and Co-Fe_2O_3-NA/$MgFe_2O_4$ heterojunction (△, ⋆) at a bias of 0.3 V (0.9 V vs. RHE) under dark (□, ○, △) and simulated sunlight irradiation (▽, ◇, ⋆). An enlarged inset of (a) is also shown in the Supporting Information, Figure S13.

obtained efficiency is also comparable to the benchmark value of 3.3 mA cm^{-2} previously reported for a IrO_2/Fe_2O_3 photoanode.[17] Higher photocurrent density indicates that better photoinduced charge generation, separation, and transport occur in the Co-Fe_2O_3-NA/$MgFe_2O_4$ heterojunction, which may be attributed to the introduction of Co^{2+} and the formation of the heterojunction. Importantly, there was no saturation of photocurrent density observed in the whole potential scan range, suggesting efficient charge separation in the heterojunction. Additionally, a remarkable cathodic shift in the onset potential (Fermi energy level) from −0.02 V (0.58 V vs. RHE) for Fe_2O_3-NA (1) to −0.17 V (0.43 V vs. RHE) for the heterojunction (3) was observed (inset of Figure 3a). This suggests a larger accumulation of electrons in the heterojunction, and reflects decreased charge recombination. This result is supported by Mott–Schottky analysis.[18] As shown in Figure 3b, a negative shift of approximately 0.33 V was observed for the heterojunction.

Figure 3c shows the corresponding photoconversion efficiency of the samples calculated using the following equation: $\eta = j_p(1.23-|V|)/I_0$ (see the Supporting Information for calculation details). A maximum photoconversion efficiency of 0.72% was observed for the 3DB Co-Fe_2O_3-NA/$MgFe_2O_4$ heterojunction at 0.07 V (0.67 V vs. RHE). In comparison, the efficiencies for Fe_2O_3-NA and Co-Fe_2O_3-NA are 0.21% at 0.01 V (0.61 V vs. RHE) and 0.34% at 0.15 V (0.75 V vs. RHE), respectively. Although the parameters of the heterojunction fabrication have not been fully optimized, this value is comparable to Fe_2O_3-based sensitized structures studied by others, who reported the maximum photoconversion efficiencies ranging from 0.6% to 0.77%.[19]

To further investigate the photoresponse of the heterojunction, the transient photocurrents of the samples were carried out during repeated ON/OFF illumination cycles at 0.5 V (1.1 V vs. RHE). All of the samples exhibited prompt and reproducible photocurrent responses upon each illumination (Figure 3d). The transient photocurrent density of the Co-Fe_2O_3-NA/$MgFe_2O_4$ heterojunction is 2.55 mA cm^{-2}, which is greatly enhanced compared to those of the Fe_2O_3-NA (0.74 mA cm^{-2}) and Co-Fe_2O_3-NA (1.27 mA cm^{-2}), respectively. We believe the 3DB structure of the heterojunction increases photocurrent density by enhancing the optical pathway and assisting in charge separation. Moreover, generation of an O_2 signal for the Co-Fe_2O_3-NA/$MgFe_2O_4$ heterojunction was observed upon illumination. The calculated Faradic efficiency is about 98% (Supporting Information, Figure S6).

To understand the role of Co-doping and $MgFe_2O_4$ sensitization on 3DB Fe_2O_3-NA, we compared the PEC performance of the different samples (Figure 3e). Both the 3DB Co-Fe_2O_3-NA/$MgFe_2O_4$ heterojunction and Co-Fe_2O_3-NA showed a great enhancement in photocurrent density after doping, which were about 1.28 and 1.37 times better than that of Fe_2O_3-NA/$MgFe_2O_4$ (2.61 mA cm^{-2}) and Fe_2O_3-NA (1.24 mA cm^{-2}) at 0.8 V, respectively. This confirms that with a proper doping level, the cobalt doping not only enhances light harvesting (Supporting Information, Figure S3), but also promotes electron transfer and reduces the recombination of photogenerated electron–hole pairs (Supporting Information, Figures S7, S8) owing to the formation of localized state dopant energy levels of Co in the band gap of Fe_2O_3.[20] Direct

evidence of the formation of the doping energy levels was obtained from valence-band XPS (Supporting Information, Figure S7). The valence-band maximum of Co-Fe_2O_3-NA is 1.97 eV below Fermi level by conventional linear extrapolation method. This value is smaller than that of Fe_2O_3-NA (2.08 eV). The valence-band edge exhibited a circa 0.11 eV red-shift after Co-doping. These results indicate that Co dopant provides additional electronic states above the valence band, which are responsible for the efficient light harvesting and separation of the charge carrier. A similar finding was also reported by Ganesh et al.[21]

The 3DB Co-Fe_2O_3-NA/$MgFe_2O_4$ heterojunction gave the highest photocurrent density of 3.34 mA cm^{-2}, which is higher than those of the Co-Fe_2O_3-NA (1.71 mA cm^{-2}) and pure $MgFe_2O_4$ (0.39 mA cm^{-2}) at 0.8 V, respectively. The value is even higher than the sum of photocurrent density for the Co-Fe_2O_3-NA and $MgFe_2O_4$, indicating that there exist a cooperative interaction between the two materials, and provides further evidence of the formation of a heterojunction. Moreover, the photocurrent density of the 3DB Co-Fe_2O_3-NA/$MgFe_2O_4$ heterojunction was approximately 77.6% higher than that of 1D Co-Fe_2O_3-NA/$MgFe_2O_4$ heterojunction (1.88 mA cm^{-2} at 0.8 V). This suggests that high contact area with the electrolyte and the excellent light-trapping characteristic (multiple scattering)[22] of the 3DB heterojunction plays a significant role in improving the PEC performance.

To further understand the enhanced charge-transfer property of the heterojunction, we conducted EIS measurements for the Fe_2O_3-NA, Co-Fe_2O_3-NA, and the 3DB Co-Fe_2O_3-NA/$MgFe_2O_4$ heterojunction. In the Nyquist diagram (Figure 3 f), the radius of each arc is associated with the charge-transfer process at the corresponding electrode/electrolyte interface; A smaller radius correlated with a lower charge-transfer resistance.[23] For all of the photoelectrodes, the arc radius under irradiation was smaller than that of in the dark. This could be attributed to a decreased charge-transfer resistance of the photoelectrodes under irradiation. Significantly, the composite material showed a smaller arc radius than that of other electrodes both in dark and under irradiation, suggesting that an effective separation of photogenerated electron–hole pairs and faster interfacial charge transfer occurred on the 3DB Co-Fe_2O_3-NA/$MgFe_2O_4$ interface owing to the formation of the heterojunction.[24] Additionally, a drastic quenching of photoluminescence intensity of 3DB Fe_2O_3-NA was observed after the introduction of Co^{2+} and $MgFe_2O_4$ (Supporting Information, Figure S8), indicating that the recombination of the photogenerated charge carriers is greatly reduced in the heterojunction. Finally, we measured the stability of the PEC performance along with its time dependence. The photocurrent density with time was highly stable for all samples tested within 1100 s of illumination (Supporting Information, Figure S9).

Considering the above results, a charge transfer mechanism for the 3DB heterojunction is proposed and illustrated in the Supporting Information, Scheme S1. As shown by the energy diagram of the 3DB Co-Fe_2O_3-NA/$MgFe_2O_4$ heterojunction, Co-Fe_2O_3-NA and $MgFe_2O_4$ have suitable and well-matched band potentials.[11] Upon irradiation, electrons are promoted from the valence bands of Co-Fe_2O_3-NA and $MgFe_2O_4$ to their respective conduction bands. The photogenerated electrons easily migrate from the conduction band of $MgFe_2O_4$ to that of the Co-Fe_2O_3-NA, driven by the band alignment, and then transport to the Ti substrate along the Co-Fe_2O_3 nanorods, which provides a direct path for electron transport. Meanwhile, holes in the valence band and impurity level of Co-Fe_2O_3 transfer to that of $MgFe_2O_4$ to react with water to form O_2.[25] The impurity level formed by Co-doping facilitates hole transport and reduces the recombination of photogenerated electron–hole pairs when the amount of doping is proper.[20] As a result, the photogenerated electron–hole pairs are effectively separated, which is crucial for the enhancement of PEC activity.

In summary, we have successfully developed a simple two-step method for the synthesis of a three-dimensional branched Co-Fe_2O_3-NA/$MgFe_2O_4$ heterojunction as a flexible photoanode for PEC water oxidation. Because of the novel 3D branched structure, the heterojunction demonstrated enhanced photocurrent density (3.34 mA cm^{-2}, AM 1.5 G), which is 2.69, 1.95, and 1.78 times higher than that of Fe_2O_3-NA, Co-Fe_2O_3-NA, and 1D Co-Fe_2O_3-NA/$MgFe_2O_4$ at 0.8 V vs. Ag/AgCl, respectively. The excellent charge transfer, enhanced light-harvesting ability, and large contact area may all contribute to the enhanced properties. Our findings open a promising avenue to developing new photoelectrodes with 3D branched structures for efficient photoelectrochemical water oxidation.

Received: September 19, 2012
Published online: December 6, 2012

Keywords: cobalt · electrochemistry · α-Fe_2O_3 · $MgFe_2O_4$ · water oxidation

[1] M. G. Walter, E. L. Warren, J. R. McKone, S. W. Boettcher, Q. X. Mi, E. A. Santori, N. S. Lewis, *Chem. Rev.* **2010**, *110*, 6446 – 6473.
[2] a) D. K. Zhong, J. Sun, H. Inumaru, D. R. Gamelin, *J. Am. Chem. Soc.* **2009**, *131*, 6086 – 6087; b) Y. Song, S. Qin, Y. Zhang, W. Gao, J. Liu, *J. Phys. Chem. C* **2010**, *114*, 21158 – 21164; c) J. Jiang, Y. Li, J. Liu, X. Huang, C. Yuan, X. W. Lou, *Adv. Mater.* **2012**, *24*, 5166 – 5180.
[3] L. Li, Y. Yu, F. Meng, Y. Tan, R. J. Hamers, S. Jin, *Nano Lett.* **2012**, *12*, 724 – 731.
[4] Y. Ling, G. Wang, D. A. Wheeler, J. Z. Zhang, Y. Li, *Nano Lett.* **2011**, *11*, 2119 – 2125.
[5] D. A. Wheeler, G. Wang, Y. Ling, Y. Li, J. Z. Zhang, *Energy Environ. Sci.* **2012**, *5*, 6682 – 6702.
[6] I. S. Cho, Z. Chen, A. J. Forman, D. R. Kim, P. M. Rao, T. F. Jaramillo, X. Zheng, *Nano Lett.* **2011**, *11*, 4978 – 4984.
[7] J. Shi, Y. Hara, C. Sun, M. A. Anderson, X. Wang, *Nano Lett.* **2011**, *11*, 3413 – 3419.
[8] K. Sun, et al., *Nanoscale* **2012**, *4*, 1515 – 1521 (see the Supporting Information).
[9] C. Singh, S. B. Narang, I. S. Hudiara, Y. Bai, K. Marina, *Mater. Lett.* **2009**, *63*, 1921 – 1924.
[10] M. T. Mayer, C. Du, D. Wang, *J. Am. Chem. Soc.* **2012**, *134*, 12406 – 12409.
[11] H. G. Kim, P. H. Borse, J. S. Jang, E. D. Jeong, O. S. Jung, Y. J. Suh, J. S. Lee, *Chem. Commun.* **2009**, 5889 – 5891.
[12] Y. Hou, X. Y. Li, Q. D. Zhao, X. Quan, G. H. Chen, *Adv. Funct. Mater.* **2010**, *20*, 2165 – 2174.

[13] Z. Wang, P. Lazor, S. K. Saxena, H. S. C. O'Neill, *Mater. Res. Bull.* **2002**, *37*, 1589 – 1602.
[14] B. Zhou, X. Zhao, H. Liu, J. Qu, C. P. Huang, *Appl. Catal. B* **2010**, *99*, 214 – 221.
[15] M. Xu, P. Da, H. Wu, D. Zhao, G. Zheng, *Nano Lett.* **2012**, *12*, 1503 – 1508.
[16] K. Sivula, F. Le Formal, M. Grätzel, *ChemSusChem* **2011**, *4*, 432 – 449.
[17] S. D. Tilley, M. Cornuz, K. Sivula, M. Grätzel, *Angew. Chem.* **2010**, *122*, 6549 – 6552; *Angew. Chem. Int. Ed.* **2010**, *49*, 6405 – 6408.
[18] Y. L. Lee, C. F. Chi, S. Y. Liau, *Chem. Mater.* **2010**, *22*, 922 – 927.
[19] a) Z. Zhang, M. F. Hossain, T. Takahashi, *Appl. Catal. B* **2010**, *95*, 423 – 429; b) P. Sharma, P. Kumar, A. Solanki, R. Shrivastav, S. Dass, V. Satsangi, *J. Solid State Electrochem.* **2012**, *16*, 1305 – 1312.
[20] Y. Cong, H. S. Park, H. X. Dang, F. R. F. Fan, A. J. Bard, C. B. Mullins, *Chem. Mater.* **2012**, *24*, 579 – 586.
[21] I. Ganesh, A. K. Gupta, P. P. Kumar, P. S. Chandra Sekhar, K. Radha, G. Padmanabham, G. Sundararajan, *Mater. Chem. Phys.* **2012**, *135*, 220 – 234.
[22] J. Liao, S. Lin, L. Zhang, N. Pan, X. Cao, J. Li, *ACS Appl. Mater. Interfaces* **2012**, *4*, 171 – 177.
[23] N. J. Bell, Y. H. Ng, A. Du, H. Coster, S. C. Smith, R. Amal, *J. Phys. Chem. C* **2011**, *115*, 6004 – 6009.
[24] Y. Hou, X. Li, Q. Zhao, X. Quan, G. Chen, *Environ. Sci. Technol.* **2010**, *44*, 5098 – 5103.
[25] A. Iwase, Y. H. Ng, Y. Ishiguro, A. Kudo, R. Amal, *J. Am. Chem. Soc.* **2011**, *133*, 11054 – 11057.

